

Nanoscale

Accepted Manuscript



This is an *Accepted Manuscript*, which has been through the Royal Society of Chemistry peer review process and has been accepted for publication.

Accepted Manuscripts are published online shortly after acceptance, before technical editing, formatting and proof reading. Using this free service, authors can make their results available to the community, in citable form, before we publish the edited article. We will replace this *Accepted Manuscript* with the edited and formatted *Advance Article* as soon as it is available.

You can find more information about *Accepted Manuscripts* in the [Information for Authors](#).

Please note that technical editing may introduce minor changes to the text and/or graphics, which may alter content. The journal's standard [Terms & Conditions](#) and the [Ethical guidelines](#) still apply. In no event shall the Royal Society of Chemistry be held responsible for any errors or omissions in this *Accepted Manuscript* or any consequences arising from the use of any information it contains.

ARTICLE

Ultrasonic-electrodepositing PtPd alloy nanoparticles on ionic liquid–functionalized graphene paper: towards flexible and versatile nanohybrid electrode

Cite this: DOI: 10.1039/x0xx00000x

Received 00th January 2012,
Accepted 00th January 2012

DOI: 10.1039/x0xx00000x

www.rsc.org/

Yimin Sun,^{*a} Huaming Zheng,^a Chenxu Wang,^b Mengmeng Yang,^b Aijun Zhou,^a and Hongwei Duan^{*b}

Here we fabricate a new type of flexible and versatile nanohybrid paper electrode by ultrasonic-electrodepositing PtPd alloy nanoparticles on freestanding ionic liquids (IL)–functionalized graphene paper, and explore its multifunctional applications in electrochemical catalysis and sensing systems. The graphene-based paper materials demonstrate intrinsic flexibility, exceptional mechanical strength and high electrical conductivity, and therefore can serve as an ideal freestanding flexible electrode for electrochemical device. Furthermore, the functionalization of graphene with IL (*i.e.*, 1-Butyl-3-methylimidazolium tetrafluoroborate) not only increases the electroactive surface area of graphene-based nanohybrid paper electrode, but also improves the adhesion and dispersion of metal nanoparticles on paper surface. These unique attributes, combined with the merits of ultrasonic-electrodeposition method, lead to the formation of PtPd alloy nanoparticles on IL–graphene paper with high loading, uniform distribution, controlled morphology and favourable size. Consequently, the resultant nanohybrid paper electrode exhibits remarkable catalytic activity as well as excellent cycle stability and improved anti-poisoning ability towards the electrooxidation of fuel molecules such as methanol and ethanol. Furthermore, for nonenzymatic electrochemical sensing of some specific biomarkers such as glucose and reactive oxygen species, the nanohybrid paper electrode shows high selectivity, sensitivity and biocompatibility in these bio-catalytic processes, and can be used for real-time tracking hydrogen peroxide secretion by living human cells. All these features demonstrate its promising application as a versatile nanohybrid electrode material in flexible and lightweight electrochemical energy conversion and biosensing systems such as bendable on-chip power source, wearable/implantable detector and *in vivo* micro-biosensors.

Introduction

The advent of recently launched flexible technologies has been considered as a revolutionary event and has attracted tremendous attention from both academic and industrial aspects.¹ Flexible portable electronic devices, such as roll-up displays, curved smart mobile phones, electronic papers, wearable and implantable biosensors, are bendable, foldable, lightweight, small in size and operationally safe, which outperform the current rigid, heavy and bulky electronic devices, and therefore are anticipated to boost the commercialization of next-generation electronic device.² As a result, significant progresses have been achieved in developing flexible electrochemical sensing system³ and energy conversion/storage unit⁴, which typically represent the integral parts of flexible electronic devices. The design of these flexible devices requires the innovation of attractive electrode materials with high activity and suitable electrode configuration that can realize full flexibility. In this sense, graphene nanosheets with unique atom-thick two dimensional structure have been considered as a preferable electrode material

because of its large surface area, electronically superior conductivity, as well as high stability in electrochemical environments. More importantly, previous studies show that individual graphene or graphene oxide nanosheets can be assembled into a macroscopic well-ordered paper-like structure.^{5–10} The as-obtained ultrathin and flexible graphene papers exhibit unique electrochemical, mechanical and interfacial properties, and are demonstrated to be an ideal binder-free and freestanding electrode for supercapacitors and lithium-ion batteries.^{11–14} Our interest in graphene papers focuses on using them as catalyst supports for noble metal nanoparticles to fabricate a versatile noble metal–graphene nanohybrid electrode for the new concepts of electrochemical application in flexible and lightweight electrochemical sensing and energy conversion systems. Up to now, several studies are reported in implantation and growth of metal nanoparticles on graphene-based substrate, or immobilization of metal nanoparticles on graphene nanosheets through self-assembly method.¹⁵ However, due to the lack of surface functional groups, the pristine surface of graphene paper is relatively inert and hence is difficult to load dense nanoparticles with

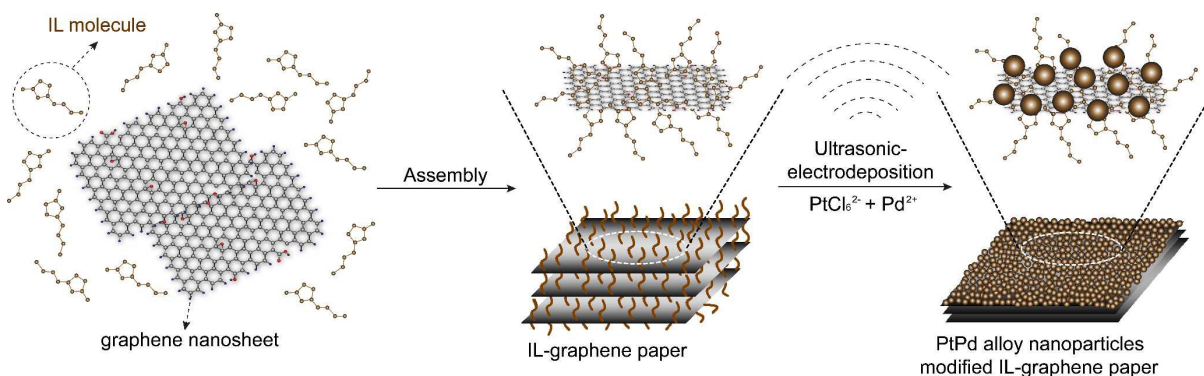


Fig. 1 Preparation process of IL-graphene paper and subsequent ultrasonic-electrodeposition of PtPd alloy nanoparticles on IL-graphene paper.

favourable size and shape. As a result, chemical modification of graphene is expected to be an effective way to improve the adhesion and dispersion of metal nanoparticles on its surface.^{16,17} Herein, we report a new type of freestanding and flexible nanohybrid electrode fabricated by ultrasonic-electrodepositing PtPd alloy nanoparticles on ionic liquid (IL)-functionalized graphene paper (IL-graphene paper), and explore its multifunctional application in electrochemical catalysis and sensing. Nowadays, passionate endeavor has been dedicated to designing and synthesizing graphene supported noble metal (*e.g.*, Pt, Pd and Au)^{9,10,18,19} and their alloy (*e.g.*, PtPd^{20,21} and PtAu²²) nanomaterials owing to their intrinsic physical and chemical properties, which gives rise to a significant improvement on the overall performance of electrocatalysis. Furthermore, IL has also attracted considerable interest for its specific properties, such as high conductivity, negligible vapor pressure, low toxicity, high thermal, chemical and electrochemical stabilities.^{23,24} In particular, IL can work well as a modifier in nanomaterials fields since the introduction of IL moieties into functional materials could improve their performance and give rise to a wide range of applications.²⁵⁻³³ Our previous results demonstrated that IL molecules could interact with graphene nanosheets through covalent and noncovalent interactions, which effectively improved the electrochemical and hydrophilic properties of the resultant IL modified graphene nanohybrid materials, making them ideal electrode materials in lightweight and flexible supercapacitor devices.³⁴⁻³⁷ In addition, the rich functional groups of IL on graphene layer could serve as active sites for anchoring metal nanoparticles. IL with low interface tension can also enhance the nucleation rate, which is favourable to form smaller particles.³⁰

In this work, the preparation process of IL-graphene paper and subsequent ultrasonic-electrodeposition of PtPd alloy nanoparticles on it are demonstrated in Fig. 1. The functionalization of graphene with IL (1-Butyl-3-methylimidazolium tetrafluoroborate, BMIMBF₄) through the cation- π interaction could effectively avoid the agglomeration of graphene nanosheets in water and increase the electroactive area of resultant graphene paper. For the ultrasonic-electrodeposition of PtPd alloy nanoparticles on it, the continuous high-intensity ultrasonic irradiation during the electrodeposition procedure leads to both chemical and physical effects such as mass-transport enhancement, surface cleaning and radical formation, which significantly restricts the aggregation and minimizes the size of the as-obtained nanoparticles.^{37,38} Collectively, the synergetic effects of IL incorporated in graphene paper and ultra-sonication during electrodeposition process enable PtPd alloy nanoparticles forming with uniform distribution, controlled morphology, and favourable size. Due to these unique attributes, the resultant nanohybrid paper electrode exhibits remarkably catalytic activity as

well as excellent cycle stability and improved anti-poisoning ability towards the electrooxidation of fuel molecules including methanol and ethanol. Furthermore, for nonenzymatic electrochemical sensing of glucose and hydrogen peroxide (H₂O₂), the nanohybrid paper electrode also shows high selectivity, sensitivity and biocompatibility in these bio-catalytic processes, which enable it to be used for real-time tracking H₂O₂ secretion by living human cells. Therefore, it is foreseeable that the proposed PtPd decorated IL-graphene nanohybrid paper electrode, which combines the nanosized electrocatalytic units and macroscopic flexible electrode architecture, will hold great promise to be used as key element in a diverse of advanced electrochemical platforms such as bendable on-chip fuel cell with high electrical efficiencies and flexible electrochemical sensor for wearable and implantable application.

Experimental

Chemicals

Hexachloroplatinic (IV) acid hexahydrate (H₂PtCl₆, purity: 99.9 %), palladium (II) chloride (PdCl₂), graphite powder (<150 μ m, 99.99% trace metals basis), IL 1-Butyl-3-methylimidazolium tetrafluoroborate (BMIMBF₄, purity: 98 %), methanol, ethanol and D-glucose (purity: \geq 99.5 %) were obtained from Aldrich. All other chemicals used were of analytical reagent grade.

Preparation of Nanohybrid Paper Electrodes

The graphite oxide was firstly synthesized from graphite powder based on a modified Hummers method.³⁹ The exfoliation of graphite oxide to graphene oxide (GO) nanosheets was achieved by ultrasonication of the dispersion for 2 h. The reduced GO (rGO) was prepared by adding 35% hydrazine aqueous solution into the as-obtained GO solution under stirring, and then heated at 95 $^{\circ}$ C for 1 h. The GO and rGO were washed with distilled water and dried under vacuum. IL and rGO (dry powder) were mixed and ground in an agate mortar to form a uniform black gel, *i.e.*, IL-functionalized rGO (IL-rGO) gel, and the ratio of IL to rGO is 50 μ L to 1 mg. The IL-rGO suspension was fabricated by transferring aforementioned IL-rGO gel into appropriate amount of distilled water, ultrasonic agitating for a few minutes to give a black suspension. IL-rGO paper (IL-rGOP) was prepared by filtrating a measured amount of IL-rGO dispersion through a membrane filter. The resulting paper-like architecture was dried in air and peeled off from the filter membrane. The thickness of the paper can be freely controlled by adjusting the volume and concentration of the suspension. Pristine rGO paper (rGOP) was prepared under the same procedure. GO paper (GOP) was fabricated according to our previous work.^{9,10}

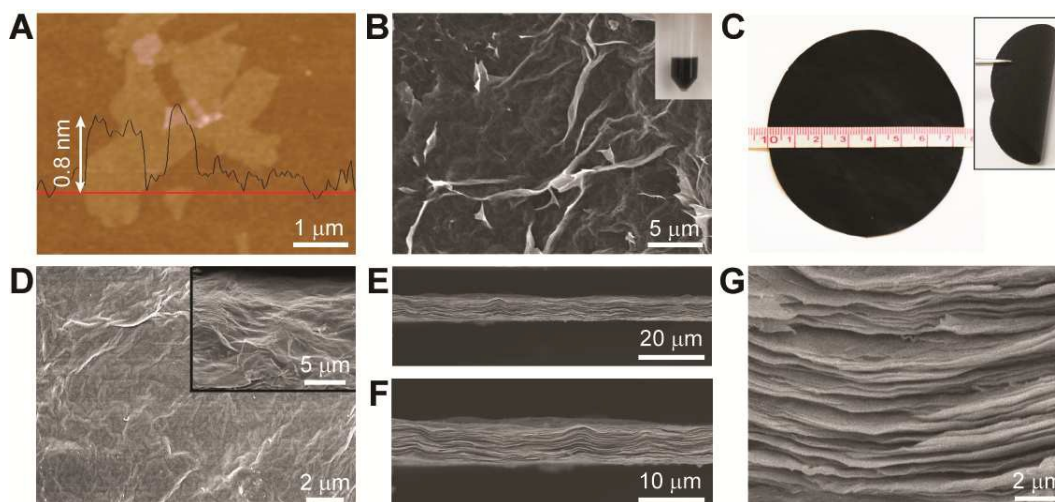


Fig. 2 (A) AFM image of rGO nanosheets. (B) SEM image of IL-rGO nanocomposite. Inset is the optical photograph of IL-rGO sample redispersed in water. (C) Optical photographs of IL-rGOP (Scale: cm). (D) SEM image of top-sectional view of IL-rGOP. Inset is the oblique-sectional view of IL-rGOP. (E–G) SEM images of cross-section of IL-rGOP with different magnifications.

The ultrasonic-electrodeposition of PtPd alloy nanoparticles on IL-rGOP was performed in 0.2 M Na_2SO_4 aqueous solution containing 0.5 mM H_2PtCl_6 and 1.0 mM PdCl_2 . The deposition time was 300 s and the potential was -0.2 V (vs. Ag/AgCl). During the potentiostatic deposition, the solution was irradiated with ultrasonic wave. The temperature of the solution was maintained at 4.0 ± 0.1 °C using an ice water bath in order to obtain smaller particles. The as-prepared electrode was denoted as PtPd/IL-rGOP (I). Pt/IL-rGOP (I), Pd/IL-rGOP (I) and PtPd/rGOP (I) were prepared through a similar method. In comparison, PtPd/IL-rGOP (II) and PtPd/rGOP (II) were fabricated under the same condition but without ultrasonic-assistance. After electrodeposition, the resultant nanohybrid paper electrodes were taken out and carefully washed with DI water to remove excessive electrolyte, dried at 50 °C in oven to remove the residual water.

Characterization

Atomic force microscopy (AFM) observation was carried out using a MFP3D microscope (Asylum Research) with a silicon cantilever operating in tapping force mode. Scanning electron microscope (SEM) image was obtained using JEOL field-emission scanning electron microscope (JSM-6700F), equipped to perform elemental chemical analysis by energy dispersive X-ray spectroscopy (EDX). X-ray diffraction (XRD) data were recorded with an X-ray diffractometer Bruker AXS D8 using Cu $K\alpha$ radiation (40 kV, 200 mA) with a Ni filter. Fourier transform infrared (FT-IR) spectra were obtained on a Perkin Elmer Spectrum One Spectrometer. Electrodeposition, electrochemical impedance spectroscopy (EIS), cyclic voltammetric (CV) and chronoamperometric (CA) experiments were performed with a CHI 660 D electrochemical workstation (CH Instrument Company). During the electrochemical measurements, the working electrode was a contacted graphene-based paper set in cell device, and the auxiliary and reference electrodes were Pt wire and Ag/AgCl, respectively.

Cell culture and testing

In this work, PtPd/IL-rGOP (I) electrode has been employed for real-time tracking H_2O_2 secretion by live cells macrophages. The cells were maintained in a culture medium consisting of Dulbecco's modified Eagle medium (DMEM) at 37°C and subcultured every 3

days. When the cells were grown to 80% confluency, they were used for the following tests. The cytotoxicity of the PtPd/IL-rGOP (I) with IL-rGOP as the control was evaluated using a standard cell counting Kit-8 (CCK-8) assay in a 96-well plate. One piece of PtPd/IL-rGOP (I) or IL-rGOP was soaked in every well and incubated with cells for 0–4 h. Afterward, CCK-8 solutions were added to each tested wells to measure the absorbance of every well at 450 nm, based on the ratio of the absorbance of the sample well to that of the control cell, the cell viability expressed as a percentage was calculated.^{9, 19} To detect the secretion of H_2O_2 by live cell, a conventional three-electrode system was adopted for the electrochemical experiments in a 24-well plate, using the graphene paper (1 cm × 0.5 cm) as the working electrode.

Results and discussion

Preparation and physicochemical characterization of IL-graphene paper

Fig. 2A shows the AFM image of the as-obtained rGO nanosheets, which exhibits a lateral dimension of several micrometers and an average thickness of about 0.8 nm. Due to its hydrophobic feature and π - π stacking interaction, the rGO samples demonstrate poor water-dispersible and easily precipitate out from solution within several days. When the rGO powders grind with imidazolium-based IL (*i.e.*, BMIMBF₄) to form a uniform black gel, the resultant IL-rGO gel could be readily redispersed in water *via* gentle ultrasonication, forming a homogeneous dispersion stable for several months (Fig. 2B inset), and the IL-rGO nanosheets reveal an unfolded flake-like structure, as shown by the SEM image in Fig. 2B. This is due to the strong interaction between IL molecules and graphene nanosheets. Imidazolium-based ILs are easily to interact with the basal plane of the graphitic surface *via* cation- π interaction.⁴⁰ Thus, the imidazolium ring on IL can strongly interact with the π -bonded surface of graphene, and prevent the overlap and disorder stacking of the exfoliated graphene layers. Furthermore, the IL (*i.e.*, BMIMBF₄) used in this work is hydrophilic in nature; therefore, the attachment of IL to the graphene plane provides a highly stable dispersibility of graphene in water. IL-rGO paper (IL-rGOP) was prepared by filtrating IL-rGO dispersion through a membrane filter. After air drying and peeling off from the filter

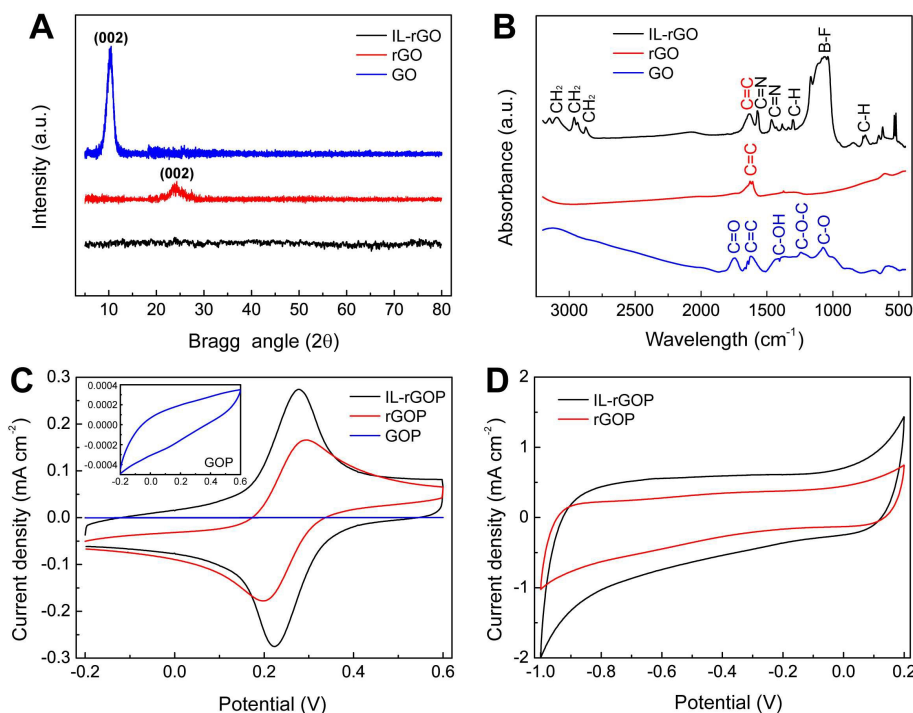


Fig. 3 (A) XRD patterns IL-rGO, rGO and GO samples (from bottom to top). (B) FT-IR spectra of IL-rGO, rGO and GO samples (from top to bottom). (C) CV curves of IL-rGOP, rGOP and GOP electrodes in 0.1 M KCl containing 1.0 mM $K_3Fe(CN)_6$ and 1.0 mM $K_4Fe(CN)_6$ (from outer to inner). Scan rate: 20 mV s^{-1} . Inset is the CV curve of GOP electrode in a magnified scale. (D) CV curves of IL-rGOP and rGOP electrodes (from outer to inner) in 0.1 M PBS (pH 7.0). Scan rate: 100 mV s^{-1} .

membrane, a freestanding IL-rGO paper was obtained, as shown in Fig. 2C. The thickness of the paper can be well controlled by adjusting the volume and the concentration of the suspension. The IL-rGOP is strong and flexible in mechanics, with a slight metallic luster on both sides (Fig. 2C inset). SEM image reveals that the surface of the IL-rGOP is quite uniform and smooth (Fig. 2D), except some corrugated and scrolled structures that resemble silk veil waves, which are intrinsic to graphene nanosheets.⁴¹ The IL-rGOP exhibits a thickness of about $5 \mu\text{m}$ through the entire cross section (Fig. 2E and 2F), where the IL-rGO nanosheets assemble into highly ordered layer-by-layer structure under vacuum filtration-induced directional flow (Fig. 2G). Tensile test measurements reveal IL-rGOP possesses acceptable mechanical strength including high values of tensile strength (124.7 MPa) and ultimate tensile strain of 1.34 % (Supplementary Information, Fig. S1).

The crystal structure, lattice constant and crystal orientation of IL-rGO together with rGO and GO samples were characterized by XRD, as shown in Fig. 3A. The characteristic diffraction peak (002) of GO at $2\theta = 10.8^\circ$ (corresponding to a interplanar d -space of 0.826 \AA) is ascribed to the introduction of oxygenated functional groups, such as epoxy, hydroxyl ($-\text{OH}$), carboxyl ($-\text{COOH}$) and carbonyl ($-\text{C}=\text{O}$) groups, on both sides and edges of the graphene sheets. The typical diffraction peak (002) of GO shifts to higher angle ($2\theta = 24.9^\circ$) after reduction by hydrazine, corresponding to a interlayer space of 0.357 \AA (JCPDS No. 41-1487).^{6, 42-44} This is because GO nanosheets are partially reduced to graphene and restacked into an ordered crystalline structure. When rGO interact with IL, this predominant peak at $2\theta = 24.9^\circ$ disappears completely, indicating that the cation- π interaction between IL and graphene has prevented the graphene nanosheets from restacking.

FT-IR spectra of IL-rGO, rGO and GO samples are shown in Fig. 3B. GO sample demonstrates the presence of $\text{C}=\text{O}$ (ν (carbonyl)) at

1750 cm^{-1} , $\text{C}=\text{C}$ (at 1620 cm^{-1}), $\text{C}-\text{OH}$ (ν (carboxyl)) at 1385 cm^{-1} , $\text{C}-\text{O}-\text{C}$ (ν (epoxy symmetrical ring deformation vibration)) at 1240 cm^{-1} , and $\text{C}-\text{O}$ (ν (epoxy or alkoxy)) at 1075 cm^{-1} , which is ascribed to the hydroxyl, epoxy and carbonyl moieties on graphene. When GO has been chemically reduced to rGO by hydrazine, the absorption bands of oxygen functionalities disappear, only the peak of $\text{C}=\text{C}$ at 1620 cm^{-1} remains, indicating that most oxygen functionalities have been removed by hydrazine. Furthermore, IL-rGO sample exhibits the presence of $\text{C}-\text{H}$, CH_2-N and CH_3-N stretching vibration centered at 3090 cm^{-1} , 2965 cm^{-1} , 2870 cm^{-1} , 1572 cm^{-1} , 1466 cm^{-1} and 1170 cm^{-1} , assigning to the vibration and imidazolium ring in plane asymmetric stretching. These fingerprint peaks, along with the strong absorption band caused by the ν ($\text{B}-\text{F}$) in BF_4^- at 1060 cm^{-1} , signify that the interactions between IL $[\text{BMIM}][\text{BF}_4]$ and graphene nanosheets enable the IL molecules to successfully graft onto graphene nanosheet and the further filtrating process does not cause the leaching of IL from the resultant IL-rGOP.

In view of the electrochemical response being highly sensitive to the physicochemical properties of the electrode surface, $\text{Fe}(\text{CN})_6^{3-/4-}$ redox probe has been selected to study the electrochemical characteristics of IL-rGOP by CV measurements with rGOP and GOP electrodes as control. As shown in Fig. 3C, no redox peaks are obtained on the GOP electrode. Since GOP electrode exhibits poor electric conductivity due to its insulating property, the application of GOP in electrochemistry is severely restricted. In comparison, a pair of quasi-reversible Faradic currents associated with the well-defined redox waves of the $\text{Fe}(\text{CN})_6^{3-/4-}$ couple can be observed on rGOP electrode, indicative of a significant increased electrochemical activity that originated from the improved electron transport properties after the conjugated sp^2 -hybridized network of GO being partially recovered. Furthermore, IL-rGOP electrode exhibits larger capacitive currents and Faradic currents than rGOP, and the peak

potential separation decreases to 50 mV, demonstrating that the introduction of IL improves the capacitive properties of IL-rGOP electrode and accelerates the heterogeneous electron transfer between the electrode and the redox species in solution. The background CV curves of IL-rGOP and rGOP in 0.1 M phosphate buffer solution (PBS, pH 7.0) show that the double layer capacitance of IL-rGOP is much higher than that of rGOP (Fig. 3D), confirming that IL-rGOP has a much higher electrochemical active area. As demonstrated by previous work, by modifying surface of graphene nanosheets with IL, each graphene nanosheets effectively stabilized via electrostatic and cation- π interaction between graphene and IL units,^{32,33} the resulting graphene sheets can be stably dispersed in aqueous and organic solution to form a homogeneous colloidal suspension due to an enhanced solubility and electrostatic inter-sheet repulsion provided by the IL units.^{27,44} Furthermore, the IL modified graphene nanomaterials have showed the higher charge transfer that was favor to exhibit an enhanced electrochemical performance.^{46,47} And the graphene aggregation by the intersheet van der Waals interaction could also be prevented because IL molecules act as "spacer" between individual graphene nanosheets.³⁴⁻³⁷ Herein, the increased electrochemical active area of IL-rGOP can probably be attributed to the richness of the hydrophilic functional groups associated with BF_4^- anion, which decreases the restacking of graphene nanosheets, enhances the hydrophilic ability and facilitates the access of solvated and charged ions.

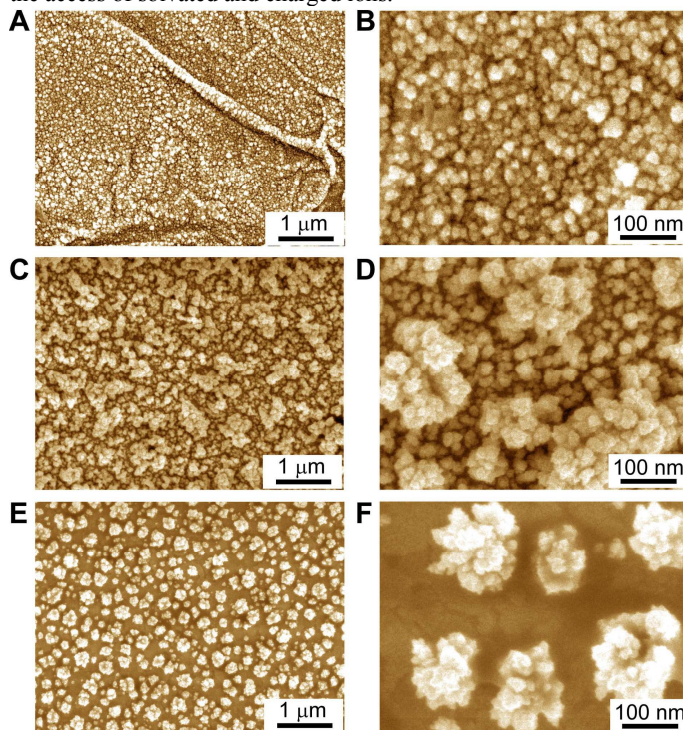


Fig. 4 SEM images of PtPd/IL-rGOP (I) (A, B), PtPd/IL-rGOP (II) (C, D) and PtPd/rGOP (II) (E, F) with different magnifications.

Electrodeposition of PtPd nanoparticles on IL-rGOP

IL-rGOP has been employed as a substrate for the electrodeposition of PtPd alloy nanoparticles. As displayed in Fig. 4A, a dense layer of well-dispersed PtPd alloy nanoparticles are deposited on the surface of IL-rGOP with the aid of sonication, which was denoted as PtPd/IL-rGOP (I). The magnified image shows that the PtPd nanoalloy on IL-rGOP has approximately spherical morphology, with a narrow size distribution of 15–20 nm (Fig. 4B). The average mass loading of PtPd alloy nanoparticles on IL-graphene paper

measured by EDX is ~5.2%, and atomic ratio of Pt/Pd is calculated to be 58:42. For comparison, the PtPd alloy nanoparticles deposited on IL-rGOP without ultrasonic agitation (denoted as PtPd/IL-rGOP (II)) exhibit rough-surface characteristic due to the obvious agglomeration of the particles (Fig. 4C and 4D). This is because the continuous high-intensity ultrasonic irradiation during electrodeposition process generate both chemical and physical effects such as mass-transport enhancement, surface cleaning and radical formation, which significantly restrict the aggregation and minimize the size of the as-obtained nanoparticles.^{37,38}

To study the effect of substrate on the density and morphology of the deposited particles, the PtPd alloy particles have also been deposited on pristine rGOP, which was denoted as PtPd/rGOP (II). As shown in Fig. 4E and 4F, due to the lack of functional groups acting as nucleation sites on rGOP, the PtPd particles on rGOP are sparse and their diameters are up to 150 nm. The changes of the nanostructure and density of PtPd particles on IL-rGOP substrate are related to the high conductivity of IL-rGOP and strong metal-support interaction between PtPd alloy particles and IL-rGOP. In principle, it has been recognized that the formation of catalytic metal (such as Pt) clusters involves two distinct stages, those are the nuclei formation of the new phase and the growth of nuclei into bigger particles with time.⁴⁸ PtPd alloy nanoparticles formed in the first step can be anchored and stabilized by the rich oxygenate group of IL on IL-rGOP. Meanwhile, IL has low interface tension and thus can enhance the nucleation rate, which is favorable to form smaller PtPd particles.³⁰

For better understanding the superior electrocatalytic effect of PtPd alloy, Pt and Pd nanoparticles have also been loaded on IL-rGOP by ultrasonic-electrodeposition, which were denoted as Pt/IL-rGOP (I) and Pd/IL-rGOP (I). Fig. 5A shows the XRD patterns of Pt/IL-rGOP (I), Pd/IL-rGOP (I) and PtPd/IL-rGOP (I) samples recorded in the 2θ range of 10–90°. The diffraction patterns for all the samples exhibit five diffraction peaks corresponding to the (111), (200), (220), (311) and (222) facets of face-centered cubic (fcc) structure crystal.⁴⁹ These indicate that Pt, Pd and PtPd alloy on IL-rGOP exist in the form of crystalline state. With respect to the diffraction peaks of Pt/IL-rGOP (I), the corresponding peaks of PtPd/IL-rGOP (I) shift to higher 2θ values. The lattice constant can be calculated from the diffraction peak position and the (111) peak has been chosen for the calculation of lattice constants.⁵⁰ The detailed structural parameters derived from XRD analysis are shown in Supplementary Information (Table S1). From which we can see that the PtPd alloy nanoparticles possess smaller lattice constant than Pt nanoparticles. This is because Pd atoms have much smaller radii than Pt atoms, the incorporation of Pd in the fcc structure of Pt causes the lattice contraction, resulting in the decrease of the lattice constant and the shift of the peaks to higher 2θ for PtPd alloy nanoparticles with respect to that of Pt nanoparticles. Assuming the validity of Vegard's Law (the linear lattice constant-concentration relation),³⁸ the estimated atomic ratio of Pt/Pd is 64:36, which is roughly consistent with that calculated from EDX. The formation of PtPd/IL-rGOP (I) was further characterized by EDX (Fig. S2), presenting the peaks corresponding to C, O, Pt, and Pd elements, confirming the existence of bimetallic PtPd alloy on IL-rGOP. The average crystallite size was calculated from the broadening of the (220) diffraction peaks using Scherrer's equation, showing that the average crystallite sizes of IL-rGOP supported Pt, PtPd and Pd nanocatalysts are 10.0, 11.1, and 8.3 nm, respectively.⁵¹ Furthermore, the particles analysis of Pt, PtPd and Pd nanocatalyst on IL-rGOP support has been conducted by SEM using image analysis software (Nano Measurer), which reveals that the average particle size for Pt/IL-rGOP (I), PtPd/IL-rGOP (I) and Pd/IL-rGOP (I) are 18, 22 and 23 nm, respectively (Fig. S3).

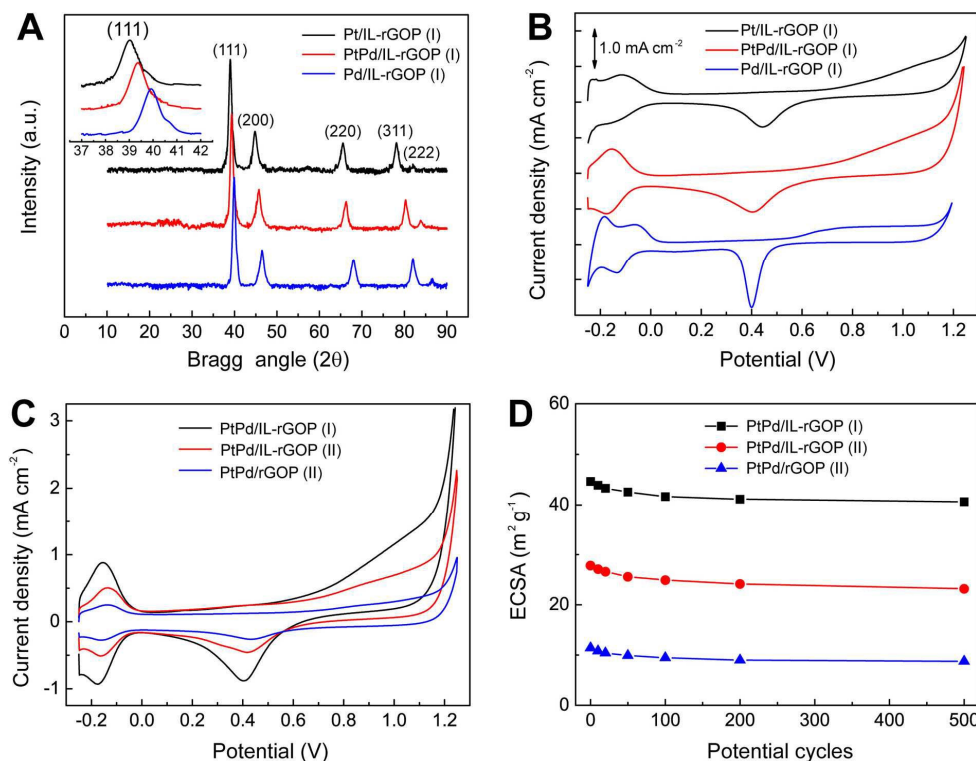


Fig. 5 (A) XRD analysis of the Pt/IL-rGOP (I), PtPd/IL-rGOP (I) and Pd/IL-rGOP (I) (from top to bottom). Inset is the regional comparison between 36° and 42° . (B) CV curves of Pt/IL-rGOP (I), PtPd/IL-rGOP (I) and Pd/IL-rGOP (I) electrodes (from top to bottom) in deaerated 0.5 M H_2SO_4 . (C) CV curves of PtPd/IL-rGOP (I), PtPd/IL-rGOP (II) and PtPd/rGOP (II) electrodes (from outer to inner) in deaerated 0.5 M H_2SO_4 . Scan rate: 50 mV s^{-1} . (D) Decay of the ECSA of PtPd/IL-rGOP (I), PtPd/IL-rGOP (II) and PtPd/rGOP (II) electrodes (from top to bottom) during potential cycles.

The CV profiles of Pt/IL-rGOP (I), PtPd/IL-rGOP (I) and Pd/IL-rGOP (I) in deaerated 0.5 M H_2SO_4 are shown in Fig. 5B. Well-defined hydrogen desorption/adsorption peaks from polycrystalline Pt (or Pd) for the formation and reduction of Pt (or Pd) oxide are observed for all the samples in the potential region from -0.25 to 0 V, indicating that Pt, Pd and PtPd nanocatalysts possess electrochemical activity. Moreover, the quasi-reversible oxidation/reduction peaks are observed in the potential range from 0.4 to 1.0 V for all the samples, which are associated with Pt and Pd, and the overlapping Pt and Pd oxide formation (generally accepted as OH_{ads} species formed from oxidation of water on Pt, Pd or PtPd alloy surfaces), as well as the reduction of oxide species on the electrode surface. A comparison of the CV curves demonstrates that the onset potentials of oxide formation on PtPd alloy are more negative than that on pure Pt. This is due to the increased donor ability and electropositive nature of alloying elements Pd.⁵²

The electrochemical activities of PtPd alloy nanocatalyst deposited on IL-rGOP with and without ultrasonic assistance are evaluated by CV experiments tested within the same potential range in deaerated 0.5 M H_2SO_4 . As seen from Fig. 5C, all the samples are electrochemically active in which the hydrogen desorption/adsorption characteristics from polycrystalline Pt (or Pd) are presented. The electrochemical active surface area (ECSA) can be estimated by the integrated charge (after excluding the double layer charging effect) in the hydrogen desorption/adsorption region. ECSA provides important information regarding the number of available active sites per gram of electrocatalyst. It accounts not only for the catalyst surface available for charge transfer, but also includes the access of a conductive path to transfer the electrons to and from the

electrode surface. The estimated ECSA increases in the order of PtPd/rGOP (II) < PtPd/IL-rGOP (II) < PtPd/IL-rGOP (I) (Fig. 5D). As the PtPd nanoparticles deposited on IL-rGOP with ultrasonic irradiation possess more uniform dispersion and higher loading comparing with those deposited on pristine rGOP or IL-rGOP without ultrasonic irradiation, it owns much more accessible active sites and larger ECSA. In electrocatalytic fields, the electrode materials with large ECSA demonstrate substantial advantages concerning mass and charge transport by providing shorter effective lengths for both electronic and ionic transport, a higher electrode/electrolyte contact area, and in some cases also interfacial local effects,^{53,54} and thereby exhibit superb electrocatalytic performance.

The stability of the electrocatalysts is one of the most important factors because of the high demand for their long-term performance, which can be investigated by repeated potential cycling in acidic solution. The results show that the PtPd/IL-rGOP (II) and PtPd/rGOP (II) lose 16.5% and 23.2% of its initial ECSA after potential cycling up to 500 cycles, whereas PtPd/IL-rGOP (I) loses only 8.9% of its initial ECSA under the same condition (Fig. 5D). The high durability is due to the presence of well-dispersive PtPd alloy nanoparticles on IL-rGOP, and the strong interactions between the nanoparticles and IL-rGOP substrate. Consequently, the results from the CV and durability tests suggest that IL-rGOP is a superior substrate material for the stable immobilization of PtPd particles.

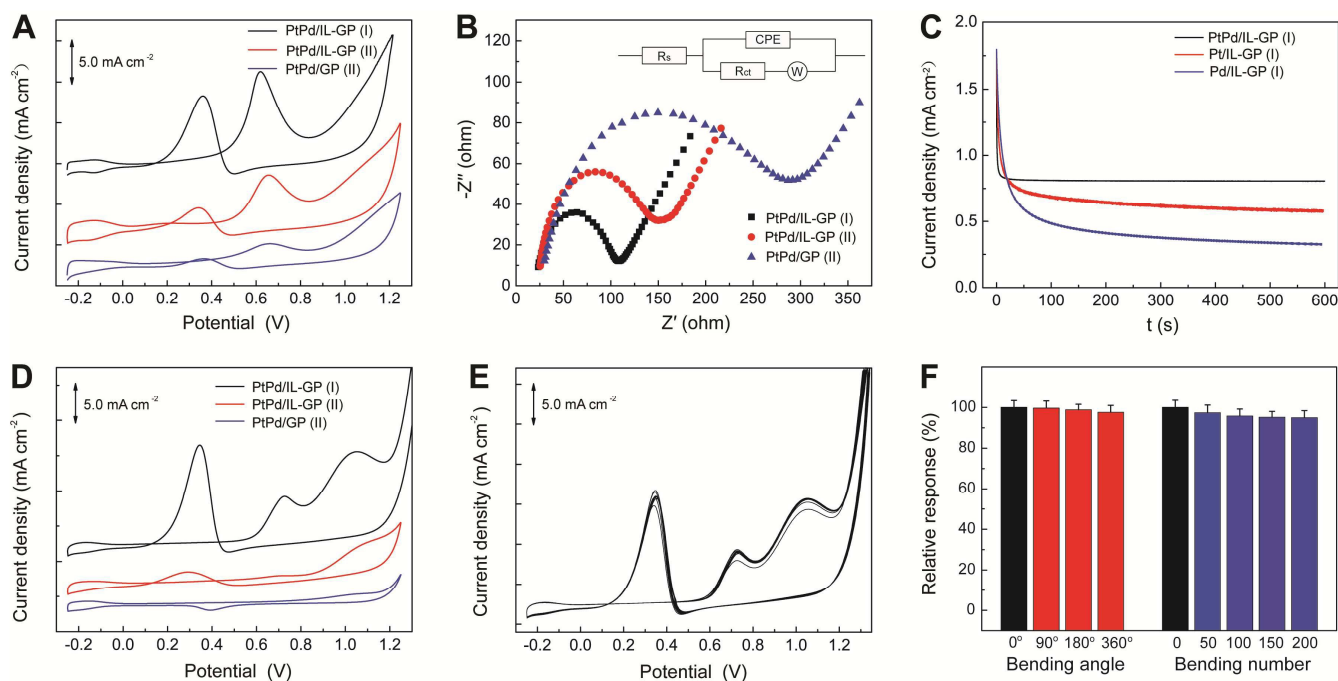


Fig. 6 (A) CV curves for methanol oxidation over PtPd/IL-rGOP (I), PtPd/IL-rGOP (II) and PtPd/rGOP (II) electrodes (from top to bottom) in 0.5 M H₂SO₄ containing 0.5 M methanol. (B) EIS for methanol oxidation over PtPd/IL-rGOP (I), PtPd/IL-rGOP (II) and PtPd/rGOP (II) electrodes (from inner to outer) in 0.5 M H₂SO₄ containing 0.5 M methanol. Inset is the equivalent circuit. Electrode potential: +0.6 V. (C) CA curves for methanol oxidation over PtPd/IL-rGOP (I), Pt/IL-rGOP (I) and Pd/IL-rGOP (I) electrodes (from top to bottom) in 0.5 M H₂SO₄ containing 0.5 M methanol. (D) CV curves for ethanol oxidation over PtPd/IL-rGOP (I), PtPd/IL-rGOP (II) and PtPd/rGOP (II) electrodes (from top to bottom) in 0.5 M H₂SO₄ containing 0.5 M ethanol. Scan rate: 20 mV s⁻¹. (E) CV curves for ethanol oxidation on PtPd/IL-rGOP (I) during potential cycling in 0.5 M H₂SO₄ containing 0.5 M ethanol. Cycle: from 1 to 20. Scan rate: 20 mV s⁻¹. (F) Relative current response of PtPd/IL-rGOP (I) upon bending inward to different angles or repeated 360° bending in 0.5 M H₂SO₄ containing 0.5 M ethanol.

Electrochemical performances of PtPd modified IL-graphene paper electrode

The as-prepared electrocatalyst loaded graphene paper electrodes have been exposed to the commonly used fuel molecules (*e.g.*, methanol and ethanol) to investigate their electrocatalytic activity. Fig. 6A displays the CV curves of PtPd/IL-rGOP (I), PtPd/IL-rGOP (II) and PtPd/rGOP (II) in 0.5 M H₂SO₄ containing 0.5 M methanol at a scan rate of 20 mV s⁻¹. It is well-known that the activities of electrocatalyst are mainly evaluated by the parameters of peak potential, onset potential, and current density. In methanol's electrooxidation mechanism on Pt sites, the onset potential is related to the breaking of C-H bonds and subsequent removal of intermediates such as CO_{ad} through oxidation with OH_{ad} supplied by Pt-OH sites or other sources.⁵⁵ The onset potential in the forward scan is around 0.45 V for PtPd/IL-rGOP (I), which is lower than those of the PtPd/IL-rGOP (II) (0.48 V) and PtPd/rGOP (II) (0.50 V). Moreover, PtPd/IL-rGOP (I) exhibits a lower peak potential of 0.60 V, which is 50 mV negative shift with respect to PtPd/IL-rGOP (II) and PtPd/rGOP (II). And the peak current densities of PtPd/IL-rGOP (I) are significantly higher than those of PtPd/IL-rGOP (II) and PtPd/rGOP (II), demonstrating a higher electrocatalytic activity for methanol oxidation on PtPd/IL-rGOP (I). The improved electrocatalytic activity is probably attributed to the higher utilization of small sized and well dispersive PtPd nanoparticles loaded on IL-rGOP by ultrasonic electrodeposition, and the stronger interactions between PtPd and the IL-rGOP support in the promotion of C-H breaking and CO_{ad} tolerance.

EIS has been employed to estimate the charge (electron and proton) transfer resistance in different electrocatalysts, which is of great importance for methanol oxidation rate. Fig. 6B shows the Nyquist plots for PtPd/IL-rGOP (I), PtPd/IL-rGOP (II) and PtPd/rGOP (II) in 0.5 M H₂SO₄ containing 0.5 M methanol. All the Nyquist plots display similar characteristics of typical semicircles at high frequencies and a straight line at a low frequency. The equivalent circuit for the nanohybrid paper electrodes are depicted in Fig. 6B inset, where R_s represents the solution resistance, CPE (constant-phase element) is the double layer capacitance, R_{ct} is the charge-transfer resistance, and W (Warburg diffusion element) is attributed to the semi-infinite diffusion of ions at the electrode/electrolyte interface.⁵⁶ As demonstrated by previous works, the R_{ct} value is a main parameter to evaluate the inherent speed of the charge-transfer step of an electrode reaction. The lower R_{ct} value means the fast charge-transfer step involved in the electrode reaction.^{57,58} The R_{ct} values obtained from simulation of the impedance spectra are calculated to be 82 Ω, 144 Ω and 305 Ω for PtPd/IL-rGOP (I), PtPd/IL-rGOP (II) and PtPd/rGOP (II), respectively, demonstrating the fastest charge transfer rate during the methanol electrooxidation at the interface of electrode/electrolyte and highest catalytic activity of PtPd/IL-rGOP (I). Meanwhile, the lower W value of PtPd/IL-rGOP (I) also reveals that the diffusion of ions in the PtPd/IL-rGOP (I) is more facile, in good agreement with CV analysis.

The durability of PtPd alloy was further evaluated with Pt and Pd electrocatalyst as control by CA measurement. Fig. 6C demonstrates the CA curves of PtPd/IL-rGOP (I), Pt/IL-rGOP (I) and Pd/IL-rGOP (I) for long-term oxidation of methanol measured in 0.5 M H₂SO₄ containing 0.5 M methanol at a constant potential. For both Pt/IL-rGOP (I) and Pd/IL-rGOP (I), the potentiostatic current decreases rapidly at the initial stage, which might be due to the formation of partially dehydrogenated intermediates species, such as CO_{ads} and CHO_{ads} that act as poisons during the methanol oxidation reaction.⁵⁴ These currents decay gradually and finally attain a pseudo-steady state. Notably, the current density of the PtPd/IL-rGOP (I) is much higher than that of Pt/IL-rGOP (I) and Pd/IL-rGOP (I) during the whole process, indicating the excellent durability and higher electrocatalytic activity of PtPd/IL-rGOP (I) with respect to Pt/IL-rGOP (I) and Pd/IL-rGOP (I). As confirmed by our XRD results, Pt and Pd have intimate contact at the atomic scale or form alloy nanoclusters with compositional homogeneity, two mechanisms are proposed for the improved CO tolerance of PtPd alloy electrocatalyst. One is the promoted mechanism (also called the bifunctional mechanism), which attributes the enhancement of CO tolerance to the facilitation of the Pt-CO_{ads} oxidation in the presence of oxophilic elements by supplying oxygen atoms required for the surface removal of CO. The metallic and oxidative states of Pd in PtPd alloy would serve as oxophilic sites for the source of oxygen to promote the electro-oxidation of CO to CO₂ through a spillover process involving OH-species formed on the oxophilic sites to CO adsorbed at the nearby Pt sites.⁵⁹ The other is the intrinsic mechanism (also called the ligand mechanism or electronic effect) attributing to a change in the electronic properties of Pt.⁴⁹ When metallic Pt has been alloyed with a transition metal such as Pd, which has a lower electronegativity than Pt, the shift in *d* electron density from Pd to Pt would lower the density of state on the Fermi level and reduce the Pt-CO bond energy, leading to the weakening of CO adsorption on Pt and the enhancement of CO tolerance.

Ethanol is another attractive fuel molecular due to its lower toxicity and price than methanol. As shown in Fig. 6D, in the forward CV scan, ethanol oxidation produces two prominent symmetric oxidation peaks corresponds to the formation of oxidized carbonaceous species. In the reverse scan, the oxidation peak is attributed to the removal of the incompletely oxidized carbonaceous species generated during the ethanol oxidation.⁶⁰ Nevertheless, both PtPd/IL-rGOP (II) and PtPd/rGOP (II) display almost featureless voltammogram with low current density values throughout comparing with the high oxidation current on PtPd/IL-rGOP (I), indicative of very low catalytic activity toward ethanol electro-oxidation.

The stability of the PtPd/IL-rGOP (I) has also been estimated by CV test during repeated potential cycling (Fig. 6E). Before recording CV, the electrode is soaked in the test solution for 10 min to allow the system reaching a stable state. It is worthy to note that ethanol electrocatalytic current of oxidation on PtPd/IL-rGOP (I) is quite stable during the potential scan. This phenomenon is different from those obtained on other Pt-based alloy such as PtRu electrocatalyst.⁶¹ According to the literatures, as the number of cycles increase, the peak potentials in both forward and reverse scan shift to higher values and the peak currents increase greatly for PtRu alloy, which result from the leaching of Ru during the cycling of the electrode between oxidizing and reducing potentials. Finally, the CV curve of PtRu alloy is found to become similar to that of pure Pt, indicating excessive loss of Ru. However, in our work, the increased number of cycles does not cause significant changes on the CV profiles in both forward and reverse scan. By the tenth cycle, the forward peak potentials are still located at the same places and the peak current

densities remain on their initial level, signifying that the prompted element Pd does not leach from PtPd alloy during the repeated cycling and PtPd alloy is in the stable status.

In view of the fact that mechanical stability of the freestanding flexible paper electrode is highly desirable characteristics for its application in manufacturing flexible electronic system, the electrochemical behaviours of PtPd/IL-rGOP (I) with respect to the CV responses under the extensive and repetitive bending have been evaluated. The results show that upon bending inward to different angles, *i.e.*, 90°, 180° and 360°, the changes of current response of PtPd/IL-rGOP (I) toward the oxidation of 0.5 M ethanol are less than 5%. Furthermore, upon repeated 360° bending from 0 to 200 times, the changes of current response are still less than 5% (Fig. 6F). These demonstrate the high flexibility and mechanical stability of PtPd/IL-rGOP (I) electrode.

Due to its outstanding electrocatalytic performance, PtPd/IL-rGOP (I) has been utilized in the abiotic catalysis for non-biological glucose fuel cells and glucose electrochemical sensor. With respect to the glucose biofuel cell or glucose sensor containing immobilised enzymes, the non-biological glucose fuel cells and glucose sensor based on the utilization of noble metal catalysts are more attractive option because of their long-term stability and biocompatibility. In the case of non-enzymatic glucose catalysis, the glucose oxidation kinetics are strongly depend on the electrode material and the crystalline orientation of the electrode surface.⁶² Our results show that in the presence of 10 mM glucose, multiple oxidation peaks are observed during the anodic potential sweep. Among different nanohybrid paper electrodes, PtPd/IL-rGOP (I) exhibits highest electrocatalytic activity toward glucose electrooxidation in terms of increased current density, lower overpotential and improved anti-poisoning ability (Fig. 7A), which alludes to the possible use as a glucose oxidation catalyst as well.

In line with the research thrust on the investigation of selectivity of the electrochemical glucose sensing devices, the influence of the major interfering species such as ascorbic acid (AA), uric acid (UA), dopamine (DA), H₂O₂ and NO₂⁻ towards the amperometric responses of glucose has been evaluated. Beneficial from the high electrocatalytic activity of PtPd/IL-rGOP (I), the electrocatalytic oxidation of glucose occurs at the relative negative oxidation potential. Therefore, even though in biological and physiological system, the redox-active species of AA, UA, DA, H₂O₂ and NO₂⁻ possess higher electron transfer rates than that of glucose, we found that at the selected applied potential (-0.28 V) of the first anodic peak attributed to the dehydrogenation of the anomeric carbon on PtPd/IL-rGOP (I), the amperometric current response of glucose is distinct, while the responses of AA, UA, DA, H₂O₂ and NO₂⁻ are negligible (Fig. 7B). Furthermore, our results have showed that upon the addition of 50.0 mM K⁺, Na⁺, Ca²⁺, Mg²⁺, Zn²⁺, Sn²⁺, Mn²⁺, Fe²⁺, Co²⁺, Ni²⁺, Al³⁺, and 10.0 mM adenine, guanine, cytosine, thymine, xanthine, hypoxanthine, cysteine, glutamine, glycine, lactamine, phenylalanine, serine and tyrosine as well, the changes of the amperometric responses of 5.0 mM glucose on Pt/IL-rGOP (I) electrode are less than 5% (Supplementary Information, Table S2). These indicate the good selectivity of PtPd/IL-rGOP (I) toward glucose electrooxidation.

The electrochemical performance of PtPd/IL-rGOP (I) has further been utilized in nonenzymatic electrochemical sensing of H₂O₂, which is usually based on the high-performance electrocatalytic electrode to substitute for natural enzyme (*e.g.*, horseradish peroxidase). As shown in Fig. 7C, H₂O₂ exhibits a pair of well-defined redox peaks on PtPd/IL-rGOP (I), the oxidation peak at +0.2 V is attributed to the electro-oxidation of H₂O₂, while the reduction peak at -0.35 V is assigned to electro-reduction of H₂O₂. The peak current densities of both oxidation and reduction on

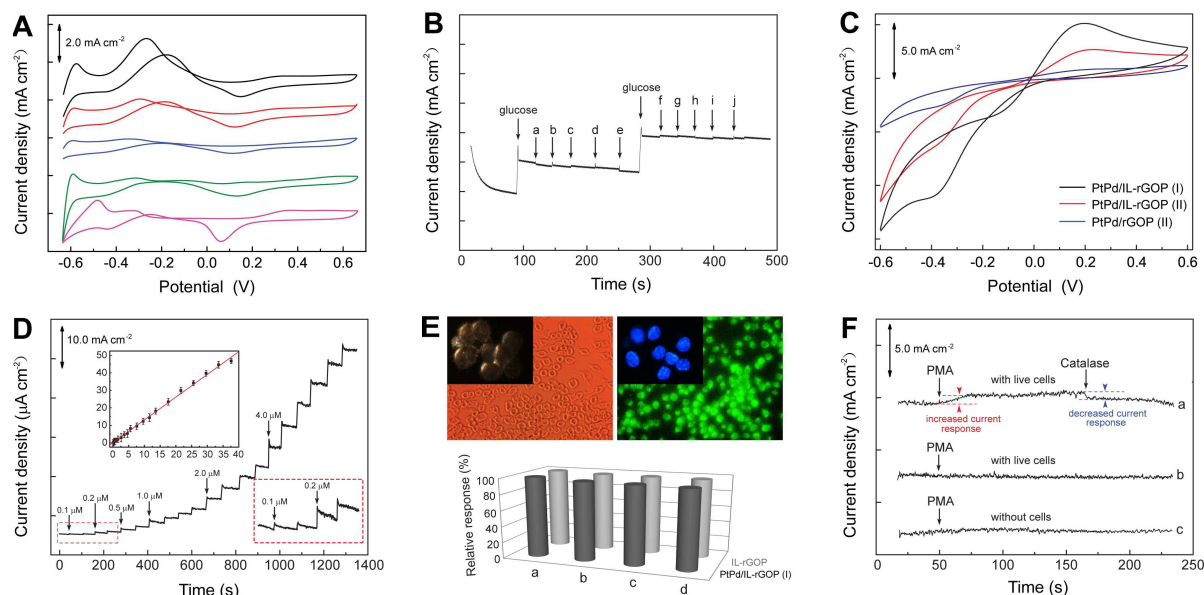


Fig. 7 (A) CV curves for glucose oxidation over PtPd/IL-rGOP (I), PtPd/IL-rGOP (II), PtPd/rGOP (II), PtPd/IL-rGOP (I), Pt/IL-rGOP (I) and Pd/IL-rGOP (I) electrodes (from top to bottom) in 0.1 M PBS (pH 7.0) containing 10 mM glucose. Scan rate: 20 mV s^{-1} . (B) Influence of 5 mM AA (a and f), 5 mM UA (b and g), 5 mM DA (c and h), 5 mM H_2O_2 (d and i) and 5 mM NO_2^- (e and j) on the amperometric response of 5.0 mM glucose in 0.1 M PBS (pH 7.0). Applied potential: -0.3 V . (C) CV curves of PtPd/IL-rGOP (I), PtPd/IL-rGOP (II) and PtPd/rGOP (II) in 0.1 M PBS (PBS) containing 1.0 mM H_2O_2 . Scan rate: 50 mV s^{-1} . (D) Amperometric responses of PtPd/IL-rGOP (I) towards successive addition of H_2O_2 . Inset of (D) is the corresponding calibration curves. Applied potential: 0.2 V . (E) Bright-field and dark-field image of macrophages with different magnifications (top), and the quantitative cell viability results obtained from the cell incubated with PtPd/IL-rGOP (I) and IL-rGOP for over 4 h (bottom). (F) Amperometric responses of PtPd/IL-rGOP (I) (a and c) and IL-rGOP (b) in 0.1 M PBS (pH 7.0) with the addition of 0.1 mM PMA and 300 U mL^{-1} catalase in the presence (a and b) and absence (c) of macrophages. Applied potential: 0.2 V .

PtPd/IL-rGOP (I) are much higher than those on PtPd/IL-rGOP (II) and PtPd/rGOP (II). Upon the successive addition of H_2O_2 into continuously stirred phosphate buffer solution (PBS, pH 7.0) at a working potential of $+0.20 \text{ V}$, the PtPd/IL-rGOP (II) electrode displays a rapid increase in amperometric current within 5 s. The linear range of the calibration curve is from $0.1 \mu\text{M}$ to $37.6 \mu\text{M}$, and the detection limit is estimated to be $0.01 \mu\text{M}$ based on signal-to-noise ratio (S/N) of 3 (Fig. 7D), which outperform those of the enzyme-based bioelectrocatalytic electrodes.⁶³⁻⁶⁶

The pathophysiological application of PtPd/IL-rGOP (I) electrode has been explored by real-time tracking H_2O_2 secretion in live cells macrophages being stimulated by phorbol 12-myristate-13-acetate (PMA). Nowadays, tremendous efforts have been stimulated toward the research of macrophages because of their important role as major effector cells in innate and adaptive immunity.⁶⁷ The bright-field and dark-field images of macrophages with different magnifications are shown in Fig. 7E. To detect the secretion of H_2O_2 by macrophages, the cells were grown in a 24-well plate to 80% confluency in 0.1 M PBS (pH 7.0). Before the electrochemical testing, the cytotoxicity of the PtPd/IL-rGOP (I) with IL-rGOP as the control was evaluated using a standard cell counting Kit-8 (CCK-8) assay in a 96-well plate. The results show that the live cells maintained $\sim 90\%$ viability after 4 h incubation with PtPd/IL-rGOP (I) and IL-rGOP (Fig. 7E), which indicates that both of these two hybrid electrodes possess high biocompatibility. Furthermore, Fig. 7F shows that upon the addition of 0.1 mM PMA, a dramatically increased amperometric current response can be observed on PtPd/IL-rGOP (I) electrode in cell well, which is up to $1.15 \mu\text{A cm}^{-2}$ within 25 s. After adding H_2O_2 scavenger catalase, the current response of H_2O_2 gradually declines to the background level. Under the same condition, the IL-rGOP electrode does not exhibit any detectable response towards the

addition of PMA in tested well containing macrophages with 80% confluency. And the control group containing no macrophages does not exhibit any response towards the addition of equal amount of PMA. These indicate that the generated amperometric current responses originated from electrochemical oxidation of H_2O_2 released from macrophages are attributed to the highly electrocatalytic PtPd alloy nanoparticles on IL-rGOP substrate, which is the essential prerequisite for tracking H_2O_2 secretion by live cells.

Conclusions

In summary, we have developed a new type of high-performance nanohybrid paper electrode based on PtPd alloy nanoparticles decorated freestanding IL-functional graphene paper by a facile and effective ultrasonic-electrodeposition method. This strategy offers several advantages: (i) Freestanding graphene-based paper with intrinsic flexibility, exceptional mechanical strength and high electrical conductivity serves as an ideal flexible electrode for advance electrochemical device. (ii) The functionalization of graphene with IL not only increases the electroactive surface area of the graphene-based nanohybrid paper electrode but also facilitates the adhesion and dispersion of metal nanoparticles on paper surface. (iii) Ultrasonic-electrodeposition procedure causes both chemical and physical effects such as mass-transport enhancement, surface cleaning and radical formation, which significantly restricts the aggregation and minimizes the size of the as-obtained PtPd nanoparticles. Therefore, PtPd alloy nanoparticles on IL-graphene paper exhibit high loading, uniform distribution, controlled morphology and favourable size. These intriguing features, combing with the synergistic effect of different components in PtPd alloy nanomaterials, make the PtPd/IL-graphene paper a versatile

electrode in electrochemical catalysis of different fuel molecules and sensing of some specific biomarkers. Therefore, we anticipate that our strategy will provide a significant step forward to bringing electrocatalytic nanoparticles–graphene hybrid electrode materials to a diverse of electrochemical applications in flexible and lightweight energy conversion device and high-performance electrochemical biosensor system.

Acknowledgements

This work was supported by the National Natural Science Foundation of China (No. 51504168), Natural Science Foundation of Hubei Province (No. 2015CFB230), and Singapore Ministry of Education Academic Research Fund Tier 3 (Project MOE2013-T3-1-002) and Arkray-NTU joint research program.

Notes and references

^a Hubei key Laboratory of Plasma Chemistry and Advanced Materials, School of Material Science and Engineering, Wuhan Institute of Technology, Wuhan, Hubei 430073, People's Republic of China

E-mail: ymsun@wit.edu.cn; ymsun1982@hotmail.com

^b School of Chemical and Biomedical Engineering, Nanyang Technological University, 70 Nanyang Drive 637457, Singapore

E-mail: hduan@ntu.edu.sg

Electronic Supplementary Information (ESI) available: Stress-strain curve of the IL-rGOP, EDX spectrum of PtPd/IL-rGOP, the particle size and size distribution of Pt, PtPd and Pd nanoparticles electrodeposited on IL-rGOP derived from SEM, and the structural parameters of Pt, PtPd and Pd nanoparticles electrodeposited on IL-rGOP derived from XRD, influence of the potential interfering species towards glucose detection. See DOI: 10.1039/b000000x/

- X. Wang, and G. Shi, *Environ. Sci.*, 2015, **8**, 790.
- Y. Shao, M. F. El-Kady, L. J. Wang, Q. Zhang, Y. Li, H. Wang, M. F. Mousaviae and R. B. Kaner, *Chem. Soc. Rev.*, 2015, **44**, 3639.
- J. Huang, Y. Zhu, X. Yang, W. Chen, Y. Zhou and C. Li, *Nanoscale*, 2015, **7**, 559.
- Y. He, W. Chen, C. Gao, J. Zhou, X. Li and E. Xie, *Nanoscale*, 2013, **5**, 8799.
- D. A. Dikin, S. Stankovich, E. J. Zimney, R. D. Piner, G. H. B. Dommett, G. Evmenenko, S. T. Nguyen and R. S. Ruoff, *Nature*, 2007, **448**, 457.
- S. Pei, J. Zhao, J. Du, W. Ren and H. M. Cheng, *Carbon*, 2010, **48**, 4466.
- S. K. Li, Y. X. Yan, J. L. Wang and S. H. Yu, *Nanoscale*, 2013, **5**, 12616.
- H. Chen, M. B. Müller, K. J. Gilmore, G. G. Wallace and D. Li, *Adv. Mater.*, 2008, **20**, 3557.
- F. Xiao, J. Song, H. Gao, X. Zan, R. Xu and H. Duan, *ACS Nano*, 2012, **6**, 100.
- F. Xiao, Y. Li, X. Zan, K. Liao, R. Xu and H. Duan, *Adv. Funct. Mater.*, 2012, **22**, 2487.
- K. Chi, Z. Zhang, J. Xi, Y. Huang, F. Xiao, S. Wang and Y. Liu, *ACS Appl. Mater. Interfaces*, 2014, **6**, 16312.
- F. Xiao, S. Yang, Z. Zhang, H. Liu, J. Xiao, L. Wan, J. Luo, S. Wang and Y. Liu, *Sci. Rep.* 2015, **5**, 9359.
- X. Zhao, C. M. Hayner, M. C. Kung and H. H. Kung, *ACS Nano*, 2011, **5**, 8739.
- K. Rana, S. D. Kim and J.-H. Ahn, *Nanoscale*, 2015, **7**, 7065.
- C. Zhu and S. Dong, *Nanoscale*, 2013, **5**, 10765.
- S. Guo, D. Wen, Y. Zhai, S. Dong and E. Wang, *ACS Nano*, 2010, **4**, 3959.
- S. Guo, S. Dong and E. Wang, *ACS Nano*, 2010, **4**, 547.
- M. Liu, R. Zhang and W. Chen, *Chem. Rev.*, 2014, **114**, 5117.
- Y. Sun, K. He, Z. Zhang, A. Zhou and H. Duan, *Biosens. Bioelectron.*, 2015, **68**, 358.
- Y. Lu, Y. Jiang, H. Wu and W. Chen, *J. Phys. Chem. C*, 2013, **117**, 2926.
- Y. Lu, Y. Jiang, W. Chen, *Nanoscale*, 2014, **6**, 3309.
- F. Xiao, Y. Li, H. Gao, S. Ge, H. Duan, *Biosens. Bioelectron.*, 2013, **41**, 417.
- S. Ernst, S. E. Norman, C. Hardacre and R. G. Compton, *Phys. Chem. Chem. Phys.*, 2014, **16**, 4478.
- T. Li, N. Li, J. Liu, K. Cai, M. F. Foda, X. Lei and H. Han, *Nanoscale*, 2015, **7**, 659.
- W. S. Chi, D. K. Roh, S. J. Kim, S. Y. Heo and J. H. Kim, *Nanoscale*, 2013, **5**, 5341.
- N. Liu, F. Luo, H. Wu, Y. Liu, C. Zhang and J. Chen, *Adv. Funct. Mater.*, 2008, **18**, 1518.
- H. Yang, C. Shan, F. Li, D. Han, Q. Zhang and L. Niu, *Chem. Commun.*, 2009, 3880.
- R. T. Kachoosangi, M. M. Musameh, I. Abu-Yousef, J. M. Yousef, S. M. Kanan, L. Xiao, S. G. Davies, A. Russell and Compton, R. G. *Anal. Chem.*, 2009, **81**, 435.
- F. Xiao, F. Zhao and B. Zeng, *Electrochem. Commun.*, 2010, **12**, 168.
- F. Xiao, F. Zhao, D. Mei, Z. Mo and B. Zeng, *Biosens. Bioelectron.*, 2009, **24**, 3481.
- M. Armand, F. Endres, D. R. MacFarlane, H. Ohno and B. Scrosati, *Nat. Mater.*, 2009, **8**, 621.
- T. Y. Kim, H. W. Lee, J. E. Kim and K. S. Suh, *ACS Nano*, 2010, **4**, 1612.
- T. Y. Kim, H. W. Lee, M. Stoller, D. R. Dreyer, C. W. Bielawski, R. S. Ruoff and K. S. Suh, *ACS Nano*, 2011, **5**, 436.
- Y. Sun, Z. Fang, C. Wang, K. R. M. Ariyawansa, A. Zhou and H. Duan, *Nanoscale*, 2015, **7**, 7790.
- Y. Sun, Y. Cheng, K. He, A. Zhou and H. Duan, *RSC Advances*, 2015, **5**, 10178.
- Y. Sun, Z. Fang, C. Wang, A. Zhou and H. Duan, *Nanotechnology*, 2015, **26**, 374002.
- H. Gao, F. Xiao, C. C. Bun and H. Duan, *ACS Appl. Mater. Interfaces*, 2011, **3**, 3049.
- F. Xiao, F. Zhao, Y. Zhang, G. Guo and B. Zeng, *J. Phys. Chem. C*, 2009, **113**, 849.
- W. S. Hummers and R. E. Offeman, *J. Am. Chem. Soc.*, 1958, **80**, 1339.
- T. Fukushima, A. Kosaka, Y. Ishimura, T. Yamamoto, T. Takigawa, N. Ishii and T. Aida, *Science*, 2003, **300**, 2072.
- G. Wang, J. Yang, J. Park, X. Gou, B. Wang, H. Liu and J. Yao, *J. Phys. Chem. C*, 2008, **112**, 8192.
- Y. Wang, Y. Li, L. Tang, J. Lu and J. Li, *Electrochem. Commun.*, 2009, **11**, 889.
- Y. X. Xu, K. X. Sheng, C. Li and G. Q. Shi, *ACS Nano*, 2010, **4**, 4324.

Journal Name

- 44 Z. Fan, K. Wang, T. Wei, J. Yan, L. Song and B. Shao, *Carbon*, 2010, **48**, 1670.
- 45 Y. Liu, Z. Xing, J. Li and X. M. Song, *Biosens. Bioelectron.*, 2011, **26**, 2632.
- 46 P. Simon and Y. Gogotsi, *Nat. Mater.*, 2008, **7**, 845.
- 47 M. Armand, F. Endres, D. R. MacFarlane, H. Ohno, B. Scrosati, *Nat. Mater.*, 2009, **8**, 621.
- 48 G. Wu, D. Li, C. Dai, D. Wang and N. Li, *Langmuir*, 2008, **24**, 3566
- 49 S. Guo, D. Wen, Y. Zhai, S. Dong and E. Wang, *ACS Nano*, 2010, **4**, 3959.
- 50 D. L. Wang, L. Zhuang and J. T. Lu, *J. Phys. Chem. C*, 2007, **111**, 16416.
- 51 C. V. Rao, A. L. M. Reddy, Y. Ishikawa and P. M. Ajayan, *Carbon*, 2011, **49**, 931.
- 52 S. Mukerjee, S. Srinivasan, M. P. Soriaga and J. McBreen, *J. Electrochem. Soc.*, 1995, **142**, 1409.
- 53 B. Seger and P. V. Kamat, *J. Phys. Chem. C*, 2009, **113**, 7990.
- 54 Y. Li, L. Tang and J. Li, *Electrochem. Commun.*, 2009, **11**, 846.
- 55 G. Wu, R. Swaidan and G. Cui, *J. Power Sources*, 2007, **172**, 180.
- 56 B. Beden, C. Lamy, N. R. D. Tacconi and A. J. Arvia, *Electrochim. Acta*, 1990, **35**, 691.
- 57 Y. Lu, and W. Chen, *J. Phys. Chem. C*, 2010, **114**, 21190.
- 58 Y. Lu and W. Chen, *ACS Catal.*, 2012, **2**, 84.
- 59 E. I. Santiago, G. A. Camara, E. A. Ticianelli, *Electrochim. Acta*, 2003, **48**, 3527.
- 60 F. Xiao, F. Zhao, J. Zeng and B. Zeng, *Electrochem. Commun.*, 2009, **11**, 1550.
- 61 W. L. Holstein and H. D. Rosenfeld, *J. Phys. Chem. B*, 2005, **109**, 2176.
- 62 Y. Chen, W. Schuhmann and A. W. Hassel, *Electrochem. Commun.*, 2009, **11**, 2036.
- 63 Y. Luo, H. Liu, Q. Rui and Y. Tian, *Anal. Chem.*, 2009, **81**, 3035.
- 64 C. X. Guo, X. T. Zheng, S. R. Ng, Y. Lai, Y. Lei and C. M. Li, *Chem. Commun.*, 2011, **47**, 2652.
- 65 X. Liu, H. Feng, J. Zhang, R. Zhao, X. Liu and D. K. Y. Wong, *Biosens. Bioelectron.*, 2012, **32**, 188.
- 66 G. Suárez, C. Santschi, O. J. F. Martin and V. I. Slaveykova, *Biosens. Bioelectron.*, 2013, **42**, 385.
- 67 C. Robert, X. Lu, A. Law, T. C. Freeman and D. A. Hume, *Immunobiology*, 2011, **216**, 1203.